Dynamics of a class-*A* nonlinear mirror mode-locked laser

A. G. Vladimirov,[1,*] A. V. Kovalev,[2,†] E. A. Viktorov,[2,‡] N. Rebrova,[3,§] and G. Huyet[4,‖]
[1]*Weierstrass Institute for Applied Analysis and Stochastics, Mohrenstrasse 39, D-10117 Berlin, Germany*
[2]*ITMO University, 14 Birzhevaya line, Saint-Petersburg, 199034, Russia*
[3]*Department of Physical Sciences, Cork Institute of Technology, Cork, Ireland*
[4]*Université Côte d'Azur, CNRS, INPHYNI, Nice, France*

(Received 10 April 2019; published 26 July 2019)

Using a delay differential equation model we study theoretically the dynamics of a unidirectional class-*A* ring laser with a nonlinear amplifying loop mirror. We perform linear stability analysis of the continuous-wave regimes in the large delay limit and demonstrate that these regimes can be destabilized via modulational and Turing-type instabilities, as well as by an instability leading to the appearance of square-waves. We investigate the formation of square waves and mode-locked pulses in the system. We show that mode-locked pulses are asymmetric with exponential decay of the trailing edge in positive time and faster-than-exponential (superexponential) decay of the leading edge in negative time. We discuss asymmetric interaction of these pulses leading to a formation of harmonic mode-locked regimes.

DOI: 10.1103/PhysRevE.100.012216

I. INTRODUCTION

The possibility of generation of short light pulses by locking the longitudinal modes of a laser was discussed only a few years after the development of the laser in 1960. Mode-locking techniques can be classified into two major classes: (1) active mode locking, based on an external modulation at a frequency close to the cavity free spectral range, and (2) passive mode locking where an intracavity nonlinear component reduces losses for pulsed operation with respect to the those of continuous-wave (CW) regime. A standard theoretical approach to study the properties of mode-locked devices is based on direct integration of the so-called *traveling wave equations* describing space-time evolution of the electric field and carrier density in the laser sections [1–4]. Another, much simpler approach limited to small gain and loss approximation was developed by Haus in [5]. To overcome this limitation the third modeling approach was suggested in Refs. [6–8] based on the lumped element method that allows one to derive a delay differential equation (DDE) model for the temporal evolution of the optical field at some fixed position in the cavity. DDE models successfully describe the dynamics of multisection mode-locked semiconductor lasers [9–14], frequency-swept light sources [15–17], optically injected lasers [18,19], semiconductor lasers with feedback [20–22], as well as some other multimode laser devices [23].

The nonlinear dynamics in mode-locked fiber lasers with a nonlinear amplifying loop mirror (NALM) are usually studied using a generalized nonlinear Schrödinger equation, which includes higher-order dispersion and Raman scattering terms [24,25] or a cubic complex Ginzburg-Landau equation [26]. The other approach is based on traveling-wave modeling, which is appropriate for a NALM laser configuration with semiconductor optical amplifier [27]. In this work, unlike the previous studies, focused on partial differential approach to model nonlinear mirror mode-locking devices, we propose and analyze a DDE model for NALM mode-locked laser. A nonlinear mirror laser as a device for ultrafast light processing was proposed in Ref. [28]. The mode-locked pulse formation mechanism in this laser is based on the asymmetric nonlinear propagation in a waveguide loop, where two counterpropagating waves acquire different intensity-dependent phase shifts caused by the Kerr nonlinearity. As a result of the interference of these waves the loop acts as a nonlinear mirror with the reflectivity dependent on the intensity of incident light. Such a nonlinear mirror plays a role similar to that of a saturable absorber in a passively mode-locked laser.

We develop a DDE laser model by assuming dispersion-free unidirectional operation inside the cavity and symmetrical beam splitting of the field into two counterpropagating fields at the entrance of the NALM. When the material variables are adiabatically eliminated, one obtains a single DDE for the complex electric field envelope, which, despite its simplicity, gives a good insight into the laser dynamics. Using this equation we find different mode-locked regimes of laser operation including square waves, ultrashort optical pulses, and their harmonics. The mode-locked pulses are always bistable with the nonlasing state and, hence, can also be considered as temporal cavity solitons or nonlinear localized structures of light [13,29]. The linear stability analysis of CW solutions corresponding to different longitudinal modes of the laser reveals modulational and Turing instabilities, as well as an instability leading to the emergence of square waves. We demonstrate analytically the mode-locked pulses are asymmetric with exponential decay of the pulse trailing

*vladimir@wias-berlin.de
†antony.kovalev@gmail.com
‡evviktor@gmail.com
§nrebrova@gmail.com
‖guillaume.huyet@inphyni.cnrs.fr

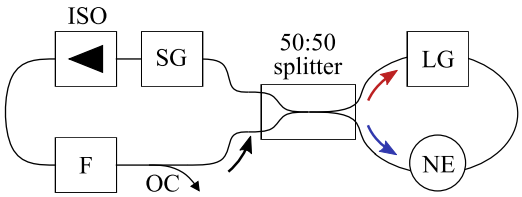

FIG. 1. Schematic view of a ring laser with a saturable gain (SG) medum, bandpass filter (F), optical isolator (ISO), output coupler (OC), and linear gain (LG) together with a nonlinear element (NE) in a Sagnac interferometer forming a NALM. Arrows show different propagation directions inside the interferometer.

tail in positive time and faster-than-exponential (superexponential) decay of the leading tail in negative time. We find that the repulsive interaction of such asymmetric pulses leads to a harmonic mode-locking regime. In order to explain the experimentally observed square wave generation recently reported in Ref. [30] in the figure-of-eight laser, we construct a one-dimensional map exhibiting a period-doubling route to chaos.

II. MODEL EQUATION AND CW SOLUTIONS

A schematic of a NALM laser with a gain and a spectral filter in an unidirectional cavity coupled to a bidirectional loop with a second gain medium and a nonlinear element, is shown in Fig. 1. This scheme corresponds to the setups studied experimentally in Refs. [30,31]. Using the approach of Refs. [7,8] we write the following DDE model for the time evolution of the electric field amplitude E and saturable gain g in a laser shown in Fig. 1:

$$\gamma^{-1}\frac{dE}{dt}+E=\sqrt{\kappa_1}e^{g/2+i\theta}\tilde{f}[|E(t-T)|^2]E(t-T), \quad (1)$$

$$\gamma_g^{-1}\frac{dg}{dt}=g_0-g-(e^g-1)|E(t-T)|^2. \quad (2)$$

Here t is the normalized time, γ is the normalized spectral filter bandwidth, κ_1 is the linear attenuation factor describing nonresonant cavity losses in the unidirectional part of the laser cavity, g_0 is the pump parameter, γ_g describes the relaxation rate of the amplifying medium, θ is the detuning parameter, and the delay parameter T is the normalized cold cavity round-trip time.

Equations (1) and (2) are similar to the model equations studied in Ref. [15] but contain an additional multiplier $\tilde{f}(|E|^2)$ in Eq. (1) describing the complex reflectivity of the nonlinear mirror introduced by the NALM. Under the simplifying assumption that the gain g is sufficiently small and the counterpropagating waves do not overlap in the nonlinear element, this multiplier can be estimated as $\tilde{f}(|E|^2)\approx\sqrt{\kappa_2}e^{G/2}(e^{i\phi_1}-e^{i\phi_2})/2$, where G and κ_2 and describe, respectively, linear amplification and losses inside the loop, while $\phi_1=\eta|E|^2/2$ and $\phi_2=\eta e^G|E|^2/2$ are the phase shifts of the clockwise and counterclockwise propagating waves indicated by arrows in Fig. 1. Since the counterclockwise propagating wave is amplified before passing through the nonlinear element, its phase shift ϕ_2 is e^G times larger than that the clockwise propagating wave, which is amplified after passing through the nonlinear element. For the gain G an equation similar to Eq. (2) can be written. Here, however, we assume for simplicity that the electric field intensity $|E|^2$ is small and the gain medium inside the NALM operates far below the saturation regime. In this case G can be considered to be a constant parameter. Furthermore, for $\phi_1=\eta|E|^2/2\ll 1$ we have $e^{\phi_1}\approx 1$, and the function $\tilde{f}$ can be rewritten in the form

$$\tilde{f}(|E|^2,G)=\sqrt{\kappa_2}e^{G/2}f(|E|^2)$$

with

$$f(|E|^2)=\tfrac{1}{2}(1-e^{ia|E|^2}), \quad (3)$$

where $a=\eta(e^G-1)/2$. Finally, for small g we replace e^g-1 with g in Eq. (2) and eliminate the gain g adiabatically, $g=g_0/[1+|E(t-T)|^2]$. Substituting this expression into Eq. (1) we get

$$\gamma^{-1}\frac{dE}{dt}+E=\sqrt{\kappa}e^{g_0/\{2[1+|E(t-T)|^2]\}+i\theta}\times f(|E(t-T)|^2)E(t-T), \quad (4)$$

where $\kappa=\kappa_1\kappa_2e^{G/2}<1$, which means that the linear gain in the NALM is balanced by the linear cavity losses, and the nonlinear function $f(|E|^2)$ is defined by Eq. (3). In the following we will show that despite being very simple, the model equation (4) is capable of reproducing such experimentally observed behaviors of nonlinear mirror lasers as mode locking and square wave generation [30]. Since our study is focused on qualitative analytical analysis of a simple model equation rather than a quantitative comparison with a particular experimental data, we restrict our consideration to the case when the adiabatic elimination of the material variables is possible.

The simplest solution of Eq. (4) is that corresponding to laser off state, $E=0$. Linear stability analysis of this trivial nonlasing solution indicates that it is always stable, which means that the laser is non-self-starting for all possible parameter values. Nontrivial CW solutions are defined by the relation

$$E=\sqrt{R}e^{i\Omega t}, \quad (5)$$

where $R=|E|^2>0$ is the intensity and Ω is the frequency of CW regime. R and Ω are the solutions of a system of two transcendental equations:

$$\kappa e^{\frac{g_0}{1+R}}\sin^2\left(\frac{aR}{2}\right)=1+\frac{\Omega^2}{\gamma^2}, \quad (6)$$

$$\tan\left(\frac{aR}{2}-T\Omega+\theta\right)+\frac{\gamma}{\Omega}=0. \quad (7)$$

Multiple solutions of these equations corresponding to different longitudinal modes of the laser are illustrated in Fig. 2(a), where CW regimes correspond to the intersections of black closed curves obtained by solving Eq. (6) and thin gray lines calculated from Eq. (7). Black curves in Fig. 2(b) show the branches of nontrivial CW solutions as functions of the pump

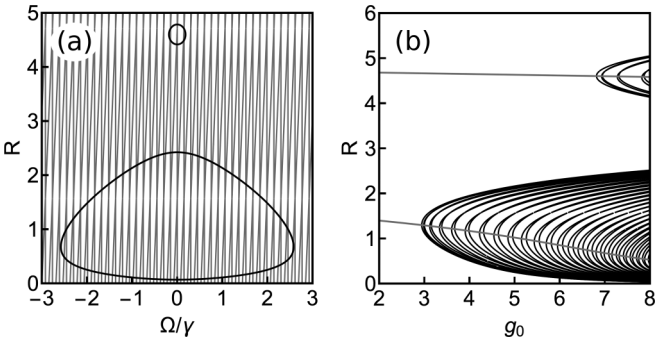

FIG. 2. (a) CW solutions at fixed pump parameter $g_0 = 5.0$. CW solutions lie on the intersections of the closed black curves [solutions of Eq. (6)] with thin gray lines [solutions of Eq. (7)]. Other parameter values: $a = 2$, $\gamma = 1$, $\kappa = 0.3$, $\theta = 0$, and $T = 20$. (b) Branches of CW solutions corresponding to different longitudinal laser modes (black lines). Two gray lines are defined by the condition (8). They intersect CW branches at the fold bifurcation points. Lower parts of the CW branches lying below the fold bifurcation points are always unstable, while upper parts can be either stable or unstable.

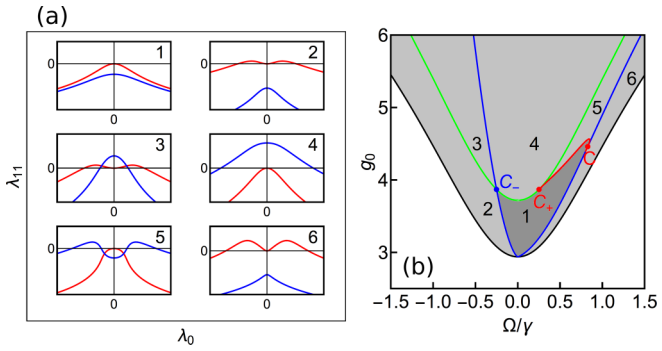

FIG. 3. (a) Two branches of pseudocontinuous spectrum. Different numbers illustrate qualitative behavior of the branches in numbered parameter domains of panel (b). (b) Bifurcation diagram on the plane of two parameters: CW frequency offset Ω and pump parameter g_0, obtained in the limit of large delay time. Black: fold bifurcation curve defined by Eq. (8), blue: modulational instability curve, which serves as a boundary of the Busse balloon and is defined by Eq. (A1) in the Appendix, green: flip instability leading to square wave appearance and defined by Eq. (12), red: Turing-type (wave) instability. $C_\pm$ are codimension-two points defined by Eqs. (13) and (14). CW solutions are stable (unstable) in the dark gray region labeled "1" (light gray regions). $\gamma = 1$ and $T \to \infty$. Other parameters are as for Fig. 2.

parameter g_0, while gray lines are defined by the condition

$$g_0 = \tilde{g} \equiv a(1+R)^2 \cot\left(\frac{aR}{2}\right). \tag{8}$$

This relation follows from the equation $\frac{dg_0}{dR} = \frac{d\Omega^2}{dR}/\frac{d\Omega^2}{dg_0} = 0$, where Ω^2 is obtained by solving Eq. (6). The intersections of the gray lines with black CW branches indicate fold bifurcation points, each of which separates the corresponding branch into two parts with the lower part being always unstable.

III. CW STABILITY IN THE LARGE DELAY LIMIT

To study linear stability the CW solutions of Eq. (4) we apply the large delay limit approach described in Ref. [32]. The large delay limit corresponds to the case when the spectral filter width is much larger than the cavity free spectral range, $\gamma T \gg 1$, so that many longitudinal modes can be excited simultaneously leading to a mode-locked regime. By linearizing Eq. (4) on a CW solution given by Eq. (5) we obtain the characteristic equation in the form

$$c_2 Y^2 + 2c_1(\lambda)Y + c_0(\lambda) = 0, \tag{9}$$

where $Y = e^{-\lambda T}$ and $c_{0,1,2}$ are given in the Appendix. In the large delay limit, $\gamma T \gg 1$, the eigenvalues belonging to the so-called *pseudocontinuous spectrum* can be represented in the form

$$\lambda = i\lambda_0 + \frac{\lambda_1}{T} + O\left(\frac{1}{T^2}\right), \quad \lambda_1 = \lambda_{11} + i\lambda_{12},$$

with real λ_0, λ_{11}, and λ_{12}. Therefore, using the approximate relations $c_{0,1}(\lambda) \approx c_{0,1}(i\lambda_0)$ and $Y \approx e^{-i\lambda_0 T - \lambda_1}$ we can solve the characteristic equation to express λ_{11} as a function of λ_0 [32]:

$$\lambda_{11}^{\pm} = \mathrm{Re}\,\lambda_1^{\pm} = \mathrm{Re}\ln(Y_\pm^{-1}),$$
$$Y_\pm = \frac{-c_1(i\lambda_0) \pm \sqrt{c_1(i\lambda_0)^2 - c_0(i\lambda_0)c_2}}{c_2}. \tag{10}$$

Two solutions $\lambda_{11}^{\pm}(\lambda_0)$ given by Eq. (10) define two branches of the pseudocontinuous spectrum shown in Fig. 3(a). Due to the phase shift symmetry of the model equation (4) $E \to Ee^{i\varphi}$ with arbitrary constant φ one of these branches is tangent to the $\lambda_{11} = 0$ axis on the $(\lambda_0, \lambda_{11})$ plane at the point $\lambda_0 = 0$, i.e., $Y_-^{-1}|_{\lambda_0=0} = 1$. Figure 3(b) shows the stability diagram of the CW solutions on the plane of two parameters: normalized frequency offset Ω/γ of a CW solution and pump rate g_0. CW solutions are stable (unstable) in the dark (light) gray domains. The black curve indicates the fold bifurcation, where two CW solutions merge and disappear. Below this curve calculated from Eqs. (6) and (8) there are no CW solutions, while above it a pair of CW solutions is born with one them corresponding to smaller intensity R being always unstable. Similarly to the case of Eckhaus instability [33,34] the upper branch of CW solutions can be stable only within the so-called Busse balloon (region labeled "1" in Fig. 3) limited from below by the modulational instability curve shown by the blue line. The modulational instability curve is defined by the condition that one of the two branches of the pseudocontinuous spectrum, which satisfies the relation $(\lambda_{11}^-)_{\lambda_0=0} = (d\lambda_{11}^-/d\lambda_0)_{\lambda_0=0} = 0$, changes the sign of its curvature at the point $\lambda_0 = 0$:

$$\left(\frac{d^2\lambda_{11}^-}{d\lambda_0^2}\right)_{\lambda_0=0} = 0. \tag{11}$$

This instability is illustrated subpanels 2 and 6 of Fig. 3(a). Explicit expression for the modulational instability condition (11) in terms of the model equation parameters is given in the Appendix.

It is seen from Fig. 3(b) that the modulational instability curve is tangent to the fold bifurcation curve at $\Omega = 0$ and that this curve becomes asymmetric with respect to the axis $\Omega = 0$ sufficiently far from the tangency point.

The upper boundary of the CW stability domain shown in Fig. 3(b) consists of two parts separated by codimension-two point C_+. The right part of this boundary lying between the points C_+ and C is indicated by red line and corresponds to the so-called Turing-type (wave) instability [32], where one of the two branches of pseudocontinuous spectrum crosses the $\lambda_{11} = 0$ axis at two symmetric points with $\lambda_0 \neq 0$, i.e., $\lambda_{11}^+ = 0$, at $\lambda_0 = \pm\lambda_0^*$ with $\lambda_0^* > 0$, see subpanel 5 of Fig. 3(a). The left part of the stability boundary lying between two symmetric codimension-two points $C_\pm$ corresponds to a flip instability leading to the appearance of square waves with the period close to $2T$. In Fig. 3(b) the flip instability curve is shown by the green line defined by the condition

$$Y_+^{-1}|_{\lambda_0=0} = -1, \tag{12}$$

which can be rewritten in the form

$$2 - \frac{g_0 R}{(1+R)^2} + aR\cot\left(\frac{aR}{2}\right) = 0. \tag{13}$$

Note, that for the case of a large, but finite, delay time, $1 \ll \gamma T < \infty$, the flip instability defined by the condition (12) is transformed into an Andronov-Hopf bifurcation with two pure imaginary eigenvalues $\lambda \approx \pm i\pi/T$. Therefore, for this case we get the relation $Y \equiv e^{-\lambda T} \approx -1$, which helps understand Eq. (12). The codimension-two points $C_\pm$ are defined by Eq. (13) together with additional conditions $(d^2\lambda_{11}^\pm/d\lambda_0^2)_{\lambda_0=0} = 0$. Using the relation (13) the additional conditions can be rewritten as

$$\Omega^2 \pm \gamma\Omega aR = \gamma^2. \tag{14}$$

An implicit equation for the coordinates of $C_\pm$ on the (Ω, g_0) plane is obtained by solving Eq. (14) for R and substituting the resulting solution into Eq. (13). It follows from Eq. (14) that the codimension-two points $C_\pm$ shown in Fig. 3(b) are symmetric with respect to $\Omega = 0$ axis. It is seen from Fig. 3(b) that the central longitudinal mode with $\Omega = 0$ is the first one undergoing a flip instability with the increase of the pump parameter g_0. The larger is the frequency offset of the mode, the higher is the flip bifurcation threshold for this mode. When, however, the positive (negative) frequency offset is sufficiently large, the mode is already unstable with respect to the Turing (modulational) instability at the flip instability point. In this case the flip bifurcation results in the appearance of unstable square waves. Note, that for any finite values of delay time, $\gamma T < \infty$, it is an Andronov-Hopf bifurcation of a CW solution that leads to the emergence of square waves. However, in the limit of infinite delay the period of the square wave regime tends to infinity, which means that the imaginary parts, $\mathrm{Im}\,\lambda \approx \pm\pi/T$, of complex eigenvalues crossing the imaginary axis at the Andronov-Hopf bifurcation tend to zero. Hence, in the limit of infinite delay we refer to this bifurcation as a flip instability corresponding to $Y = e^{\lambda T} \to -1$ in the limit $T \to \infty$; see Eq. (12).

Let us consider the CW solution of Eq. (4) corresponding to the central longitudinal mode with zero detuning from the central frequency of the spectral filter, $\Omega = 0$. For this solution the two quantities $Y_\pm$ in Eq. (10) take the form

$$Y_-|_{\Omega=0} = 1 - i\frac{\lambda_0}{\gamma}, \tag{15}$$

$$Y_+|_{\Omega=0} = \frac{1 - i\lambda_0/\gamma}{1 + aR\cot\left(\frac{aR}{2}\right) - \frac{g_0 R}{(1+R)^2}}. \tag{16}$$

From Eq. (15) we get the relations $Y_-^{-1}|_{\Omega=0,\lambda_0=0} = 1$ and $|Y_-^{-1}|_{\Omega=0,\lambda_0\neq 0} < 1$ meaning that the first branch of the pseudocontinuous spectrum of the central longitudinal mode is always stable and is tangent to the imaginary axis at $\lambda_0 = 0$. On the other hand, from Eq. (16) we see that the fold bifurcation of the central longitudinal mode defined by the condition $Y_+^{-1}|_{\Omega=0,\lambda_0=0} = 1$ coincides with Eq. (8). Similarly the flip instability responsible for the emergence of square waves is defined by the condition $Y_+^{-1}|_{\Omega=0,\lambda_0=0} = -1$ coinciding with Eq. (13). As will be shown in the next section, the condition (13) defines also the period-doubling bifurcation of a 1D map, which we construct in the next section to study the square wave formation in the DDE model (4).

IV. 1D MAP AND SQUARE WAVES

The existence of stable square wave solutions in Eq. (4) can be demonstrated by constructing a 1D map [35–37] that exhibits a period-doubling bifurcation corresponding to the emergence of square waves in the DDE model (4). To this end we rescale the time $\tau = t/T$ in Eq. (4) and obtain

$$\varepsilon\frac{dE}{d\tau} + E = \sqrt{\kappa}e^{g_0/\{2[1+|E(\tau-1)|^2]\}+i\theta} f[|E(\tau-1)|^2]E(\tau-1), \tag{17}$$

where in the large delay limit we have $\varepsilon \equiv 1/\gamma T \ll 1$. By discarding the time derivative term, which is proportional to the small parameter ε, we transform this equation into a complex map, which describes the transformation of the electric field envelope E after a round trip in the cavity and resembles the well-known Ikeda map [38]. Then, taking modulus square of both sides, we obtain a 1D map for the intensity R:

$$R_{n+1} = h(R_n), \quad h(R_n) = \kappa e^{\frac{g_0}{1+R_n}}\sin^2\left(\frac{aR_n}{2}\right)R_n, \tag{18}$$

where $R_n \equiv R(n)$ $(n = 0, 1, 2, \dots)$ with fixed points $R_n = R^*$ satisfying the condition $R^* = h(R^*)$:

$$\kappa e^{\frac{g_0}{1+R^*}}\sin^2\left(\frac{aR^*}{2}\right) = 1. \tag{19}$$

Graphical representation of the function h is given in Fig. 4(a). Note that since Eq. (19) is equivalent to Eq. (6) taken at $\Omega = 0$, which satisfies Eq. (7), fixed points of the map (18) have the intensity R coinciding with that of the central longitudinal mode, i.e., the CW solution of Eq. (4) with zero frequency offset $\Omega = 0$ from the central frequency of the spectral filter. Furthermore, for sufficiently large g_0 a stable fixed point of the map (18) exhibits a period-doubling bifurcation, which is defined by

$$1 - \frac{g_0 R^*}{(1+R^*)^2} + aR^*\cot\left(\frac{aR^*}{2}\right) = -1, \tag{20}$$

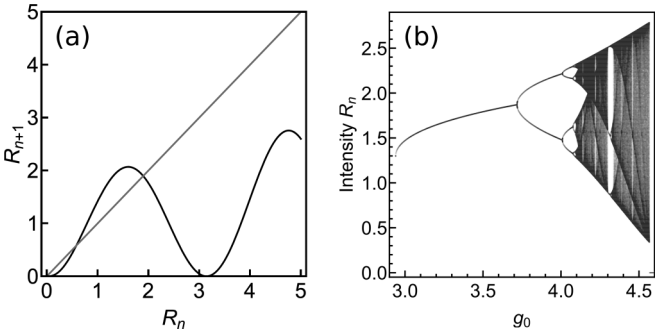

FIG. 4. (a) Graph of the function h defined by Eq. (18). Two period-one fixed points of the map correspond to the intersections of the black curve with straight gray line $R_{n+1} = R_n$. These fixed points correspond to the CW solutions of Eq. (4) lying on the upper and lower parts of the CW branch with zero frequency offset $\Omega = 0$. $a = 2$, $\kappa = 0.3$, and $g_0 = 3.8$. (b) Bifurcation diagram illustrating period-doubling route to chaos in the map (18) with $a = 2$ and $\kappa = 0.3$.

together with (19). Since the relations (19) and (20) are equivalent to (6) and (12) evaluated at $\Omega = 0$, the period-doubling bifurcation point of the map (18) coincides in the limit of large delay with the flip instability to square waves of the central longitudinal mode having zero frequency offset, $\Omega = 0$. It is seen from Fig. 4(b) that after the first period-doubling bifurcation the 1D map (18) demonstrates a period-doubling transition to chaos.

The period-doubling route to chaos obtained by numerical integration of the DDE model (4) is illustrated in Fig. 5(a), where local maxima of the electric field intensity time trace are plotted versus increasing values of the pump parameter g_0. It is seen that the diagram in this figure is very similar to that obtained with the 1D map (18); cf. Fig. 4. Note, however, that the period-doubling threshold is slightly higher in Fig. 5 than in Fig. 4. This can be explained by taking into consideration that in the DDE model (4) the threshold of the flip instability leading to the emergence of square waves increases with the absolute value of the frequency detuning Ω. Therefore, we can conclude that in Fig. 5 the CW solution undergoing the period-doubling cascade must have a small nonzero frequency detuning, $\Omega \neq 0$. The first period-doubling bifurcation in Fig. 4(a) is responsible for the formation of square waves

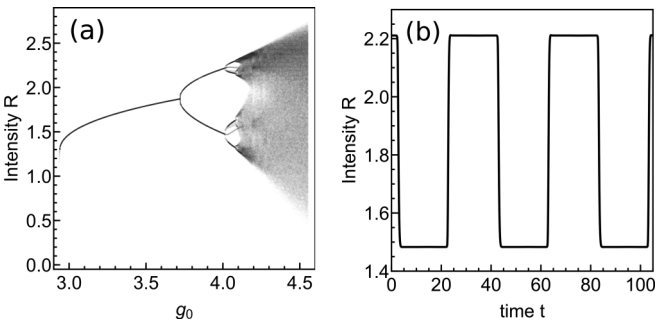

FIG. 5. (a) Bifurcation diagram obtained by numerical integration of Eq. (4) with $\kappa = 0.3$, $a = 2$, $\theta = 0$, $T = 20$, and $\gamma = 5$. (b) Square waves calculated numerically for $g_0 = 4.0$.

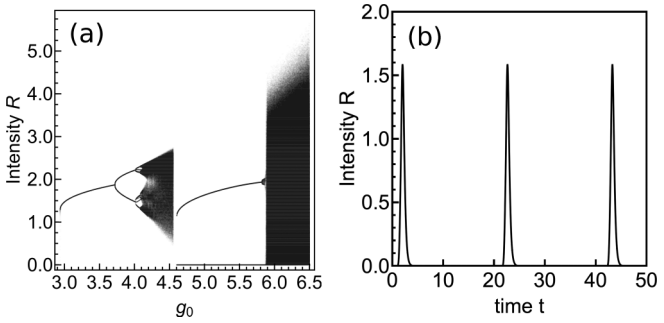

FIG. 6. (a) Bifurcation diagram obtained by numerical integration of Eq. (4). (b) Fundamental mode-locked regime with the repetition period close to the cavity round-trip time calculated for $g_0 = 5.0$. Other parameters are the same as for Fig. 5.

shown in Fig. 4(b), while further period doublings give rise to more complicated square wave patterns with larger periods. Finally, we note that with the increase of the gain parameter g_0 new pairs of fixed points of the map (18) appear in saddle-node bifurcations. For example, the second pair of fixed points corresponds to the second (right) maximum of the function h shown in Fig. 4(a) and to additional branches of CW solutions visible in the upper right part of Fig. 2(b).

V. MODE LOCKING

The bifurcation diagram in Fig. 6(a) was obtained by numerical integration of Eq. (4). It is similar to that shown in Fig. 5, but spans a larger range of the pump parameter values. It follows from this diagram that with the increase of the pump parameter g_0 after a chaotic regime associated with the period-doubling cascade the phase trajectory of the system jumps to an isolated branch of pulsed solutions with time-periodic laser intensity. This solution corresponding to a fundamental mode-locked regime with the repetition period close to the cavity round-trip time, T, is illustrated in Fig. 6(b), where it is seen that the leading edge of the pulses is much steeper than the trailing edge. In the following, we will show that unlike the trailing tail of the pulses, which decays exponentially, their leading tail demonstrates faster-than-exponential (superexponential) decay in negative time.

Let us consider a mode-locked solution of Eq. (4) with time-periodic intensity $|E(t)|^2 = |E(t + T_0)|^2$, where the period T_0 is close to the cavity round-trip time T. For this solution satisfying the condition $E(t) = E(t + T_0)e^{i\Delta}$ with a phase shift Δ we can write

$$E(t - T) = E(t - T + T_0)e^{i\Delta} \equiv E(t + \delta)e^{i\Delta}, \qquad (21)$$

where $\delta = T_0 - T > 0$ is the small difference between the solution period and the delay time. Substituting (21) into (4) we get a time advance equation [36,37],

$$\gamma^{-1}\frac{dE}{dt} + E = \frac{\sqrt{\kappa}}{2}e^{g_0/\{2[1+|E(t+\delta)|^2]\}+i\Theta} \times f[|E(t + \delta)|^2]E(t + \delta), \qquad (22)$$

where $\Theta = \theta + \Delta$. Note, that unlike the original DDE model (4), which has the stable trivial solution $E = 0$, the trivial solution of Eq. (22) is a saddle with one stable and an infinite

number of unstable directions. The stable direction determines the decay rate of the trailing tail of mode-locked pulses, while unstable directions are responsible for the decay of the leading tail in negative time. To perform a linear stability analysis of the trivial solution of Eq. (22) we write the following equation linearized at $E = 0$:

$$\gamma^{-1}\frac{dE}{dt} + E = \epsilon E(t+\delta)e^{i\Theta}, \tag{23}$$

where the linear time advance term in the right-hand side proportional to the small perturbation parameter ϵ describes an imperfection introduced by a slight asymmetry of the coupler between the laser cavity and the NALM. The spectrum of Eq. (23) is defined by

$$\lambda_k = -\gamma\left[1 + \frac{W_k(-\epsilon\gamma\delta e^{-\gamma\delta+i\Theta})}{\gamma\delta}\right], \tag{24}$$

where W_k denotes the kth branch of multivalued Lambert function. In particular, in the limit $\epsilon \to 0$ the eigenvalue with the index $k = 0$ is the only stable and negative one $\lambda_0 \to -\gamma < 0$. This eigenvalue determines the decay rate of the trailing tail of mode-locked pulses. The remaining eigenvalues with $k \neq 0$ have positive real parts diverging in the limit $\epsilon \to 0$, $\mathrm{Re}\,\lambda_k \to +\infty$. Among these unstable eigenvalues, depending on the value of Θ, which depends on the detuning parameter θ in Eq. (4), one of the two eigenvalues $\lambda_{\pm1}$ with $k = \pm1$ has the smallest real part. All other eigenvalues with $|k| > 1$ have larger real parts. Hence, for small nonzero ϵ generically one of the two eigenvalues $\lambda_{\pm1}$ determines the decay rate of the pulse leading tail in negative time. The fact that this eigenvalue tends to infinity as $\epsilon \to 0$ suggests that this decay is superexponential.

Finally let us discuss briefly the interaction of asymmetric mode-locked pulses shown in Fig. 6(b). When integrating the model equation (4) numerically it is possible to seed two or more nonequidistant pulses in the laser cavity as an initial condition. Then the pulses start to interact locally via their decaying tails. The asymmetric nature of these tails suggests that similarly to the case discussed in Ref. [39] local interaction of nonequidistant pulses will be very asymmetric as well. This can be seen in Fig. 7 illustrating an interaction of two asymmetric pulses of Eqs. (4) on the time-round-trip number plane. We see that two initially nonequidistant pulses repel each other and tend to be equidistantly spaced in the long-time limit. Furthermore, when the two pulses are sufficiently close to one another, the exponentially decaying trailing tail of the left pulse repels noticeably the right pulse, while the superexponentially decaying leading tail of the right pulse almost does not affect the position of the left pulse. When the pulses become equidistant the forces acting on a pulse from opposite directions balance each other, and a stable harmonic mode-locking regime with two pulses per cavity round trip time is established.

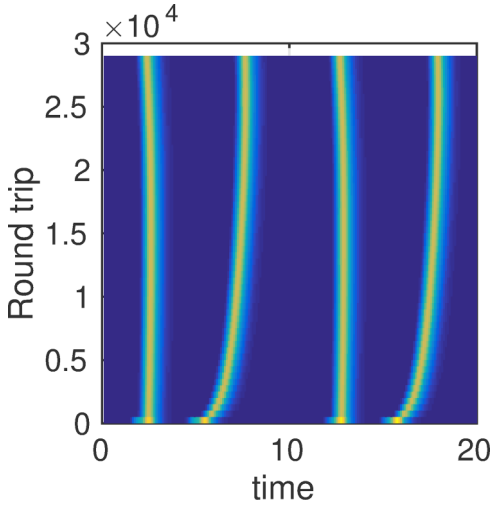

FIG. 7. Interaction of two mode-locked pulses leading to a harmonic mode-locked regime with two pulses per cavity round trip. A common drift of the two interacting pulses is eliminated. $T = 10$. The time axis spans the interval $2T$. Other parameters are the same as for Fig. 5.

VI. CONCLUSION

We have considered a simple DDE model of a unidirectional class-*A* ring NALM mode-locked laser. Linear stability analysis in the large delay limit revealed that similarly to the well-known Eckhaus instability only those CW solutions which belong to the Busse balloon can be stable. This balloon is limited from below by the modulational instability boundary. We demonstrated that with the increase of the pump parameter CW regimes lose their stability either via a Turing-type instability or through a flip instability leading to a formation of stable square waves. We have constructed a 1D map which describes the transition to square waves and their secondary bifurcations giving rise to a more complicated square wave patterns with larger and larger periods. We have shown that mode-locked pulses, which appear after a chaotic square-wave dynamics, have a exponentially decaying trailing tail and a leading tail, which decays superexponentially in negative time. When two or more pulses circulate in the laser cavity, the interaction of these pulses is repulsing and very asymmetric leading to a formation of harmonic mode-locked regimes. It is noteworthy that the mode-locked regimes considered here are always non-self-starting, which means that the pulses are sitting on a stable laser-off solution, and one needs to apply a finite perturbation to excite them. Hence, these pulses can be viewed as temporal cavity solitons having similar properties to spatial and temporal localized structures of light observed in bistable optical systems.

ACKNOWLEDGMENTS

The authors thank D. Turaev for useful discussions. A.V.K. and E.A.V. acknowledge the support by the Government of the Russian Federation (Grant No. 08-08). A.G.V. acknowledges the support of the Fédération Doeblin CNRS and subproject B5 of the DFG Project No. SFB 787.

APPENDIX

The coefficients $c_0(\lambda)$, $c_1(\lambda)$, and c_2 in the characteristic equation (9) are defined by

$$c_0(\lambda) = (\gamma - \lambda)^2 + \Omega^2,$$

$$c_1(\lambda) = -\frac{a\lambda R(R+1)^2\Omega + \gamma(\gamma-\lambda)[R(2R+4-g_0)+2] + \Omega^2[R(2R+4-g_0)+2]}{(R+1)^2} - aR\cot\left(\frac{aR}{2}\right)(\gamma^2 - \gamma\lambda + \Omega^2),$$

$$c_2 = \frac{\gamma^2\kappa e^{\frac{g_0}{R+1}}}{2(R+1)^2}\{aR(R+1)^2\sin(aR) - [R(R+2-g_0)+1][\cos(aR)-1]\}.$$

The modulational instability condition (11) of the CW solutions of Eq. (4) can be rewritten in the following form:

$$\frac{[a(1+R)^2\Omega + \gamma(\tilde{g}-g_0)]^2}{(\gamma^2+\Omega^2)^2} + \frac{2(1+R)^2\Omega^2\left[g_0^2 + 2a^2(1+R)^4 - g_0^2\cos(aR) - 2ag_0(1+R)^2\sin(aR)\right]}{R(\tilde{g}-g_0)(\gamma^2+\Omega^2)^2[1-\cos(aR)]} = 0. \tag{A1}$$

[1] B. Tromborg, H. E. Lassen, and H. Olesen, IEEE J. Quantum Electron. **30**, 939 (1994).
[2] E. A. Avrutin, J. H. Marsh, and E. L. Portnoi, IEE Proc.-Optoelectron. **147**, 251 (2000).
[3] U. Bandelow, M. Radziunas, J. Sieber, and M. Wolfrum, IEEE J. Quantum Electron. **37**, 183 (2001).
[4] U. Bandelow, M. Radziunas, A. G. Vladimirov, B. Hüttl, and R. Kaiser, Opt. Quant. Electron. **38**, 495 (2006).
[5] H. Haus, IEEE J. Sel. Top. Quantum Electron. **6**, 1173 (2000).
[6] A. G. Vladimirov and D. V. Turaev, Radiophys. Quant. Electron. **47**, 769 (2004).
[7] A. G. Vladimirov, D. Turaev, and G. Kozyreff, Opt. Lett. **29**, 1221 (2004).
[8] A. G. Vladimirov and D. Turaev, Phys. Rev. A **72**, 033808 (2005).
[9] E. A. Viktorov, P. Mandel, A. G. Vladimirov, and U. Bandelow, Appl. Phys. Lett. **88**, 201102 (2006).
[10] D. Rachinskii, A. G. Vladimirov, U. Bandelow, B. Hüttl, and R. Kaiser, J. Opt. Soc. Am. B **23**, 663 (2006).
[11] A. G. Vladimirov, U. Bandelow, G. Fiol, D. Arsenijević, M. Kleinert, D. Bimberg, A. Pimenov, and D. Rachinskii, J. Opt. Soc. Am. B **27**, 2102 (2010).
[12] R. Arkhipov, A. Pimenov, M. Radziunas, D. Rachinskii, A. G. Vladimirov, D. Arsenijević, H. Schmeckebier, and D. Bimberg, IEEE J. Sel. Top. Quant. Electron. **99**, 1100208 (2013).
[13] M. Marconi, J. Javaloyes, S. Balle, and M. Giudici, Phys. Rev. Lett. **112**, 223901 (2014).
[14] E. A. Viktorov, T. Habruseva, S. P. Hegarty, G. Huyet, and B. Kelleher, Phys. Rev. Lett. **112**, 224101 (2014).
[15] S. Slepneva, B. Kelleher, B. O'Shaughnessy, S. P. Hegarty, A. G. Vladimirov, and G. Huyet, Opt. Express **21**, 19240 (2013).
[16] S. Slepneva, B. O'Shaughnessy, B. Kelleher, S. P. Hegarty, A. G. Vladimirov, H.-C. Lyu, K. Karnowski, M. Wojtkowski, and G. Huyet, Opt. Express **22**, 18177 (2014).
[17] A. Pimenov, S. Slepneva, G. Huyet, and A. G. Vladimirov, Phys. Rev. Lett. **118**, 193901 (2017).
[18] N. Rebrova, G. Huyet, D. Rachinskii, and A. G. Vladimirov, Phys. Rev. E **83**, 066202 (2011).
[19] A. Pimenov, E. A. Viktorov, S. P. Hegarty, T. Habruseva, G. Huyet, D. Rachinskii, and A. G. Vladimirov, Phys. Rev. E **89**, 052903 (2014).
[20] B. Kelleher, M. J. Wishon, A. Locquet, D. Goulding, B. Tykalewicz, G. Huyet, and E. A. Viktorov, Chaos **27**, 114325 (2017).
[21] C. Otto, K. Lüdge, A. G. Vladimirov, M. Wolfrum, and E. Schöll, New J. Phys. **14**, 113033 (2012).
[22] L. C. Jaurigue, B. Krauskopf, and K. Lüdge, Chaos **27**, 114301 (2017).
[23] E. A. Viktorov, P. Mandel, and G. Huyet, Opt. Lett. **32**, 1268 (2007).
[24] J. M. Dudley, G. Genty, and S. Coen, Rev. Mod. Phys. **78**, 1135 (2006).
[25] A. F. J. Runge, C. Aguergaray, R. Provo, M. Erkintalo, and N. G. R. Broderick, Opt. Fiber Tech. **20**, 657 (2014).
[26] M. Salhi, A. Haboucha, H. Leblond, and F. Sanchez, Phys. Rev. A **77**, 033828 (2008).
[27] D. Chaparro and S. Balle, Phys. Rev. Lett. **120**, 064101 (2018).
[28] N. Doran and D. Wood, Opt. Lett. **13**, 56 (1988).
[29] F. Leo, S. Coen, P. Kockaert, S.-P. Gorza, P. Emplit, and M. Haelterman, Nat. Photonics **4**, 471 (2010).
[30] A. Aadhi, A. V. Kovalev, M. Kues, P. Roztocki, C. Reimer, Y. Zhang, T. Wang, B. E. Little, S. T. Chu, D. J. Moss, Z. Wang, E. Viktorov, and R. Morandotti, Proc. SPIE **10518**, 105180M (2018).
[31] M. Kues, C. Reimer, B. Wetzel, P. Roztocki, B. E. Little, S. T. Chu, T. Hansson, E. A. Viktorov, D. J. Moss, and R. Morandotti, Nat. Photonics **11**, 159 (2017).
[32] S. Yanchuk and M. Wolfrum, SIAM J. Appl. Dyn. Syst. **9**, 519 (2010).
[33] L. S. Tuckerman and D. Barkley, Physica D **46**, 57 (1990).
[34] M. Wolfrum and S. Yanchuk, Phys. Rev. Lett. **96**, 220201 (2006).
[35] S.-N. Chow and J. Mallet-Paret, in *Coupled Nonlinear Oscillators*, edited by J. Chandra and A. C. Scott, North-Holland Mathematics Studies Vol. 80 (Elsevier, North-Holland, 1983), pp. 7–12.
[36] S. N. Chow, X. B. Lin, and J. Mallet-Paret, J. Dyn. Differ. Eq. **1**, 3 (1989).
[37] M. Nizette, Phys. Rev. E **70**, 056204 (2004).
[38] K. Ikeda, Optics Commun. **30**, 257 (1979).
[39] A. G. Vladimirov, S. V. Gurevich, and M. Tlidi, Phys. Rev. A **97**, 013816 (2018).